

## Modeling multiple quantum barrier effects and reduced electron leakage in red-emitting laser diodes

M. R. Brown, R. J. Cobley, K. S. Teng, P. Rees, S. P. Wilks et al.

Citation: *J. Appl. Phys.* **100**, 084509 (2006); doi: 10.1063/1.2362906

View online: <http://dx.doi.org/10.1063/1.2362906>

View Table of Contents: <http://jap.aip.org/resource/1/JAPIAU/v100/i8>

Published by the [American Institute of Physics](#).

---

### Additional information on J. Appl. Phys.

Journal Homepage: <http://jap.aip.org/>

Journal Information: [http://jap.aip.org/about/about\\_the\\_journal](http://jap.aip.org/about/about_the_journal)

Top downloads: [http://jap.aip.org/features/most\\_downloaded](http://jap.aip.org/features/most_downloaded)

Information for Authors: <http://jap.aip.org/authors>

## ADVERTISEMENT



**FIND THE NEEDLE IN THE  
HIRING HAYSTACK**

Post jobs and reach  
thousands of hard-to-find  
scientists with specific skills



<http://careers.physicstoday.org/post.cfm> **physicstoday JOBS**

# Modeling multiple quantum barrier effects and reduced electron leakage in red-emitting laser diodes

M. R. Brown,<sup>a)</sup> R. J. Cobley, K. S. Teng, P. Rees, and S. P. Wilks

*Multidisciplinary Nanotechnology Centre, The School of Engineering, University of Wales Swansea, Singleton Park, Swansea SA2 8PP, United Kingdom*

A. Sobiesierski, P. M. Smowton, and P. Blood

*School of Physics and Astronomy, Cardiff University, The Parade, Cardiff CF24 3YB, United Kingdom*

(Received 16 May 2006; accepted 3 August 2006; published online 27 October 2006)

Severe electron leakage impedes the full exploitation of AlGaInP laser diodes in the 630 nm regime. Such thermally activated currents are attributed to inherently small conduction band offsets and intervalley transfer between the  $\Gamma$  and X conduction band minima. To negate the detrimental effect of these two intrinsic material issues a theoretical model is proposed. A multi-quantum-barrier (MQB) structure able to inhibit both  $\Gamma$ - and X-band transmissions is inserted in the  $p$ -doped region adjacent to the active region of the device, allowing a greater percentage of injected electrons to be reflected back within the active region. The design of the MQB follows a strict optimization procedure that takes into account fluctuations of superlattice layer width and composition. This model is used in conjunction with a dual conduction band drift-diffusion simulator to enable the design of the MQB at an operating voltage and hence account for nonlinear charge distribution across it. Initial results indicate strong agreement between experimentally determined effective enhancements and those predicted theoretically. © 2006 American Institute of Physics.

[DOI: [10.1063/1.2362906](https://doi.org/10.1063/1.2362906)]

## I. INTRODUCTION

Red-emitting AlGaInP quantum-well laser diodes have a huge scientific and industrial market potential with applications as varied as optical storage, short-haul communication networks, and as sources in projection television. Visible laser diodes with wavelengths down to 650 nm are routinely manufactured but as the wavelength is further reduced the lasers exhibit high threshold currents, low output power, and poor thermal characteristics. These performance issues can be attributed to the intrinsically small conduction and valence band edge discontinuities between the  $(\text{Al}_x\text{Ga}_{1-x})_y\text{In}_{1-y}\text{P}$  alloys used to generate the waveguide and cladding regions of laser devices. This inadequacy allows a considerable fraction of injected electrons to escape the laser active region and leak into the adjacent cladding layers of the device.<sup>1,2</sup>

One solution employed to combat the conduction band offset issue has been the introduction of a multi-quantum-barrier (MQB) into the  $p$ -doped cladding region adjacent to the active region of the device.<sup>3</sup> The MQB consists of alternating layers of narrow and wide band-gap semiconductor materials. This periodic arrangement results in a potential profile that instigates the formation of allowed and forbidden carrier states analogous to that of a crystal lattice<sup>4</sup> but over a much shorter range. By shrewd tuning of the periodicity of the MQB superlattice, an electron forbidden miniband may be judiciously positioned directly upon the intrinsic band edge. This effectively enhances the conduction band offset between the  $p$ -type cladding and the active region of the

device and can lead to improved carrier confinement within the waveguide regions and subsequently improve laser performance. Initial studies conducted on a range of III-V superlattices<sup>3,5,6</sup> have predicted effective enhancements in excess of 50% of the intrinsic band discontinuity, highlighting the attraction of using MQBs in AlGaInP laser diodes.

However, there has been limited success in the practical incorporation of AlGaInP MQB structures. Many groups have reported experimental evidence for improved device performance;<sup>7-9</sup> however, most recognize a disparity between enhancements found experimentally and those predicted theoretically.<sup>10-12</sup> In a previous publication,<sup>13</sup> we suggested that discrepancies between theoretical and experimental findings may be attributed to two oversimplifications in the simulations employed, namely, (i) the omission of an intervalley transport mechanism and (ii) neglecting to optimize the MQB at the working bias of the device.

The first issue is related solely to the material properties of the AlGaInP alloy. For the most part, calculation of the reflectivity/transmission probability for a particular MQB comprised of various alloys of the  $(\text{Al}_x\text{Ga}_{1-x})_y\text{In}_{1-y}\text{P}$  material is conducted assuming single valley transport, i.e., via the direct  $\Gamma$  band.<sup>6,12,14,15</sup> However,  $(\text{Al}_x\text{Ga}_{1-x})_y\text{In}_{1-y}\text{P}$  switches from being a direct to an indirect semiconductor as the aluminum content  $x$  exceeds 56%.<sup>16,17</sup> Thus, as the constituent well and barriers of a MQB typically comprise of aluminum contents between 0–0.3 and 0.7–1, respectively, there is a significant possibility of elastic scattering of electrons between the  $\Gamma$  and X minima at each heterojunction across the MQB. Experimental investigations<sup>2,18</sup> of AlGaInP laser devices found that the dominant leakage contribution comes from electrons escaping via the X-band minimum. Thus in-

<sup>a)</sup>Electronic mail: [m.r.brown@swan.ac.uk](mailto:m.r.brown@swan.ac.uk)

tervalley transport should be included within the numerical model and used to deduce a MQB structure capable of reflecting both  $\Gamma$  and  $X$  electrons.<sup>13</sup>

The second point is related to the band bending that occurs under device operation. Many authors assume flat-band conditions across the MQB. Although this is a good first approximation, it becomes inadequate at the working bias of the AlGaInP device where high injection currents distort the energy bands and subsequently the positioning of the nonallowed minibands predicted. Thus, it is essential to design the MQB under working conditions to maximize its influence and minimize distortion effects.

In a previous paper,<sup>13</sup> these two issues were accounted for, but comparison of effective enhancements found experimentally and that numerically predicted revealed an overestimation in the enhancement magnitude. In this paper, we present a more sophisticated model able to calculate the relative positioning of the bands more rigorously and predict effective enhancements within 3 meV of that found experimentally.<sup>19</sup>

The paper is set out as follows: In Sec. II, the previous numerical model<sup>13</sup> and predicted results are briefly reviewed. Experimental measurements of the effective enhancement associated with a laser device containing the MQB detailed in Sec. II are presented in Sec. III, and a comparison between experimental and theoretical enhancements is given. In Secs. IV and V, a more robust numerical model is developed, and the optimization procedure used to generate MQBs that exhibit stable reflectivity spectra are presented, respectively. We show how predicted results from this model corroborate with existing experimental data in Sec. VI. Additionally, the updated numerical model is used to predict a MQB structure with superior characteristics than that proposed previously. Finally, a summary of the results presented is given in Sec. VII.

## II. PREVIOUS NUMERICAL MODEL

The former model<sup>13</sup> solves Poisson's equation by an explicit integration technique to predict the position and nonlinear charge distribution across both the  $\Gamma$  and  $X$  conduction bands at zero bias. Due to the inherent inaccuracy of this technique it was only possible to model a small region of the whole laser device, namely, the active and surrounding  $n$ - and  $p$ -type cladding regions (i.e., regions 6–10 in Table I), with the MQB embedded in the latter. A dopant and width dependent bias was applied linearly across the structure to imitate lasing conditions of the device. Two coupled time-independent Schrödinger equations were solved under the effective-mass approximation (detailed below in Sec. IV), allowing the reflection and transmission probabilities from a particular MQB structure to be determined. The MQB is then optimized (see Sec. V) by iteratively refining its layer widths to achieve the most stable enhancement.

The resulting optimized MQB (MQB 1 hereafter) has the following layer dimensions: three initial thick material layers of 150, 150, and 96 Å width, respectively, where the first and third layers constitute quantum barriers of composition of  $(\text{Al}_{0.7}\text{Ga}_{0.3})_{0.48}\text{In}_{0.52}\text{P}$  and are separated by a quantum well of

TABLE I. Layer structure of the modeled device.

Layer No.	Material composition	Width (Å)	Doping ( $\text{cm}^{-3}$ )
1	GaAs	6 000	$5^{18}$ , $p$ type
2	$\text{Ga}_{0.49}\text{In}_{0.51}\text{P}$	100	$2^{18}$ , $p$ type
3	$(\text{Al}_{0.7}\text{Ga}_{0.3})_{0.5}\text{In}_{0.5}\text{P}$	5 000	$5^{17}$ , $p$ type
4	$(\text{Al}_{0.4}\text{Ga}_{0.6})_{0.5}\text{In}_{0.5}\text{P}$	5 000	$5^{17}$ , $p$ type
5	$(\text{Al}_{0.7}\text{Ga}_{0.3})_{0.5}\text{In}_{0.5}\text{P}$	9 000	$5^{17}$ , $p$ type
6	$(\text{Al}_{0.51}\text{Ga}_{0.49})_{0.5}\text{In}_{0.5}\text{P}$	945	$5^{17}$ , $p$ type
7	MQB Region	~900	Undoped, $p$ type
8	$\text{Ga}_{0.49}\text{In}_{0.51}\text{P}$	68	Undoped, $p$ type
9	$(\text{Al}_{0.3}\text{Ga}_{0.7})_{0.5}\text{In}_{0.5}\text{P}$	900	Undoped, $p$ type
10	$(\text{Al}_{0.51}\text{Ga}_{0.49})_{0.5}\text{In}_{0.5}\text{P}$	945	$5^{17}$ , $n$ type
11	$(\text{Al}_{0.7}\text{Ga}_{0.3})_{0.5}\text{In}_{0.5}\text{P}$	10 000	$5^{17}$ , $n$ type
12	$\text{Ga}_{0.49}\text{In}_{0.51}\text{P}$	100	$2^{18}$ , $n$ type
13	GaAs	6 000	$5^{18}$ , $n$ type

composition of  $(\text{Al}_{0.3}\text{Ga}_{0.7})_{0.48}\text{In}_{0.52}\text{P}$ . These thick initial layers inhibit low-energy tunneling of both the  $\Gamma$  and  $X$  electrons.<sup>13</sup> The optimized superlattice of MQB 1 comprises six alternate well/barrier pairs of composition of  $(\text{Al}_{0.3}\text{Ga}_{0.7})_{0.48}\text{In}_{0.52}\text{P}/(\text{Al}_{0.7}\text{Ga}_{0.3})_{0.48}\text{In}_{0.52}\text{P}$ , where each individual layer is 42 Å in width. A band profile of the active and optimized MQB regions (MQB 1) at an operating bias of 2 V is displayed in Figs. 1(a) and 1(b), where the latter dia-

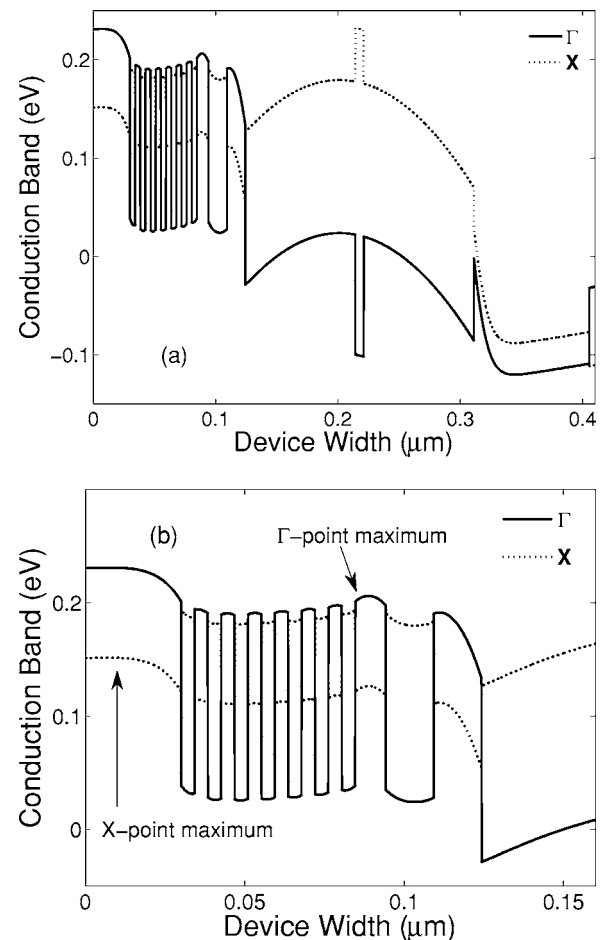


FIG. 1. Position of the  $\Gamma$  and  $X$  conduction bands at an applied voltage of 2 V. (a) Active and adjacent  $p$  and  $n$  doped cladding regions. (b) Magnification of the MQB 1 region.

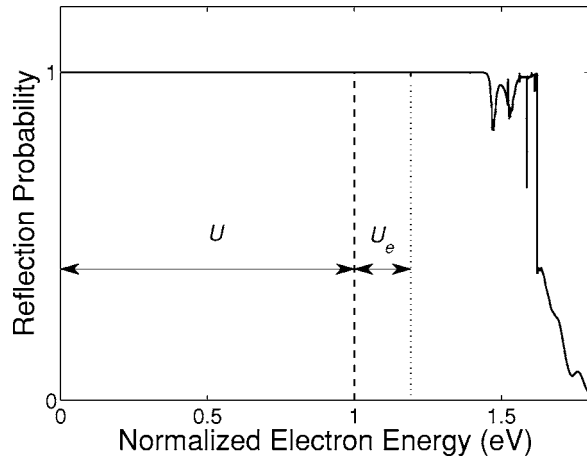


FIG. 2. Calculated normalized reflection probability of MQB 1. The reflectivity is normalized with respect to the X-band maximum indicated in Fig. 1(b) and is denoted here by  $U$ . The effective enhancement to the barrier height is indicated by  $U_e$ . The magnitude of  $U_e$  is 20% greater than of the intrinsic barrier height  $U$ . Conversion of this magnitude to eV reveals an enhancement of 25 eV to the X-band maximum.

gram shows a magnification of the MQB region and indicates the X-point maximum below which all incident electrons are classically reflected. The predicted normalized total (sum of the  $\Gamma$  and X) reflectivity spectrum of the MQB shown in Fig. 1(b) is displayed in Fig. 2. The reflectivity is normalized with respect to X-band maximum indicated in Fig. 1(b) and is denoted here by  $U$ . The effective enhancement to the barrier height is indicated by  $U_e$ . The magnitude of  $U_e$  is 20% that of the intrinsic barrier height  $U$ . Conversion of this magnitude to eV reveals an enhancement of 25 eV to the X-band maximum.

It is worth highlighting the point that this and subsequent enhancements are quite small, due to the fact that the intrinsic conduction band offsets are inherently small and that we are reducing these further by allowing intervalley transport to occur from the marked X-band maximum in agreement with experimental evidence.<sup>2,18</sup>

### III. EXPERIMENTAL DATA

Experimental work conducted by Sobiesierski *et al.*<sup>19</sup> compared the performance of a laser structure incorporating MQB 1 and a reference laser structure. The whole MQB region in the reference laser was replaced with a layer of equivalent refractive index. This measure was taken to ensure that there was no change in the optical guiding and that any observed differences were due to the effect of the MQB

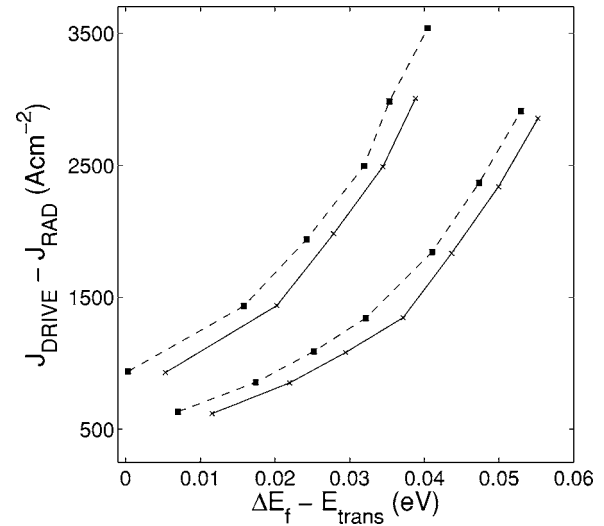


FIG. 3. Drive current density minus radiative current density as a function of quasi-Fermi level separation for the MQB (crosses) and control device (squares) at 340 K (solid) and 360 K (dashed).

on the electrical properties. The material composition, width, and doping concentration for each layer across the laser device are detailed in Table I, and Table II displays important AlGaInP material parameters used within the numerical models described in Secs. II and IV. The experimental analysis concentrated on lasers of two lengths, namely, 320 and 450  $\mu\text{m}$  long. It was shown via threshold current measurements that lasers incorporating MQB 1 had lower threshold currents at high temperature, but the same threshold current at low temperature, compared with the control for both lengths, indicating that the MQB suppressed thermally activated leakage currents.

Furthermore, to substantiate these results against other factors that might influence threshold currents, detailed analysis was performed using the segmented contact method.<sup>20</sup> This allows the modal gain, internal optical mode loss, spontaneous emission, and quasi-Fermi level separation as a function of drive current density to be determined.

This in-depth analysis revealed that the reduction in threshold current density at high temperatures achieved by incorporating MQB 1 was indeed due to a decrease in the thermally activated leakage current, and furthermore allows the magnitude of the effective enhancement to be determined. In Fig. 3, the thermally activated leakage current density derived from the difference between the drive current density and the radiative current density is plotted as a function of quasi-Fermi level separation for the MQB 1 (crosses)

TABLE II. Important AlGaInP alloy simulation parameters.  $x$  refers to the aluminum content.

Parameter	$\Gamma$ electron	X electron	Hole
Band gap (eV)	$1.91 + 0.61x^a$	$2.242 + 0.022x^b$	...
Effective mass ( $m/m_0$ )	$0.1079 + 0.036x^b$	$0.35^b$	$0.4443 + 0.015x^b$
Mobility ( $\text{cm}^2 \text{V}^{-1} \text{s}^{-1}$ )	$525 - 100x^b$	$170^b$	$7^b$
Relative permittivity	$\epsilon_0(11.76 - 0.954x)^b$ where $\epsilon_0 = 8.854 \times 10^{-12} \text{ F m}^{-1}$		
Electron affinity (eV)	$4.07 + 1.424 + 0.25x - 6.92 - (1.91 + 0.61x)^b$		

<sup>a</sup>Reference 16.

<sup>b</sup>Reference 17.



and the control device (squares) at 340 K (solid) and 360 K (dashed). The control curves are separated from the curves for MQB 1 at both temperatures by the same constant value of energy, corresponding to the value of the effective barrier enhancement. Calculating this difference yields an effective increase to the intrinsic conduction band offset of 5 meV. Comparison of this experimental value with that predicted theoretically indicates an overestimation in the latter.

Theoretical tests on the reflection calculation (detailed in Sec. IV below) were conducted but made little difference to the discrepancy between these two values, implying that the position and bending of the bands play a stronger role in the MQB's operation. This implies that the approximation of these effects by the solution of Poisson's equation alone is a first approximation but a better physical model is necessary.

In the following section we describe a more rigorous model used to predict the energy band position at applied bias and the stringent MQB optimization procedure em-

ployed to locate the most stable structure is detailed. But first we review the method used to take account of elastic intervalley scattering.

#### IV. UPDATED NUMERICAL MODEL

To simulate intervalley transport across the MQB material interfaces a scattering matrix method is utilized<sup>21,22</sup> to solve two coupled time-independent Schrödinger equations, under the effective-mass approximation. Coupling of these two equations is mediated by the inclusion of an additional term (mixing parameter) in each potential operator. The mixing parameter accounts for the magnitude of elastic scattering between  $\Gamma$  and  $X$  minima across each heterointerface. Under the assumption of parabolic bands this equation set may be expressed as

$$\hat{T}Z + \hat{V}Z = EZ, \quad (1)$$

where  $E$  is the eigenenergy of the system. The kinetic and potential operators are given by

$$\hat{T}(z) = \begin{pmatrix} -(\hbar^2/2)(\partial/\partial z)[1/m_\Gamma(z)](\partial/\partial z) & 0 \\ 0 & -(\hbar^2/2)(\partial/\partial z)[1/m_X(z)](\partial/\partial z) \end{pmatrix}, \quad (2)$$

$$\hat{V}(z) = \begin{pmatrix} V_\Gamma(z) & \alpha\delta(z) \\ \alpha\delta(z) & V_X(z) \end{pmatrix}, \quad (3)$$

respectively, where  $\hbar$  is the reduced Planck's constant,  $m_\Gamma$  and  $m_X$  are the effective electron masses at the  $\Gamma$  and  $X$  points,  $\alpha$  is the intervalley mixing parameter,  $\delta(z)$  is the Dirac-delta function, and  $V_\Gamma$  and  $V_X$  are the band offset discontinuities for the  $\Gamma$  and  $X$  minima. The off-diagonal terms  $\alpha\delta(z)$  quantify the intervalley transfer potentials ( $V_{\Gamma X}$  and  $V_{X\Gamma}$ ). The wave function spinor  $Z$  is then

$$Z(z) = \begin{pmatrix} \zeta_\Gamma(z) \\ \zeta_X(z) \end{pmatrix}, \quad (4)$$

where  $\zeta_\Gamma(z)$  and  $\zeta_X(z)$  are the  $\Gamma$  and  $X$  wave functions, respectively. Equations (1)–(4) are solved via a transfer matrix routine<sup>3,5</sup> that evolves the wave functions across the MQB structure, allowing the reflection and transmission probabilities for each band to be calculated and hence effective barrier enhancement to be determined. We refer to this routine as the reflection calculation (RC). The magnitude of the mixing parameter  $\alpha$  has been experimentally determined by Landheer *et al.*<sup>23</sup> to be 0.155 eV Å for the GaAs/AlAs/GaAs material system. By employing this value, favorable comparisons with more sophisticated pseudopotential models of Marsh<sup>24,25</sup> and Marsh and Inkson<sup>26</sup> and a similar model by Morrison and Lambkin<sup>22</sup> for the AlGaInP material system have been found. For the remainder of this study we have assumed a similar magnitude for the mixing parameter for the AlGaInP alloys as a first approximation. In Secs. V and VII, it is shown that if a stable MQB structure can be deter-

mined from the optimization procedure varying the mixing parameter by 30% has no effect on the predicted reflectivity profiles.

The second equation set, referred to as the modified drift-diffusion (MDD) set, replaces the more simplistic explicit Poisson solver used previously.<sup>13</sup> The MDD takes account of the nonlinear charge distribution across the whole laser device via solution of Poisson's equation and three carrier continuity equations (i.e.,  $\Gamma$  and  $X$  electrons and hole) simultaneously<sup>27,28</sup> utilizing Fermi-Dirac statistics.<sup>29,30</sup> This equation set may be expressed as

$$\frac{\partial}{\partial z} \left[ \epsilon(z) \frac{\partial \psi(z)}{\partial z} \right] = -q[p(z) - n^\sigma(z) + N_T(z)], \quad \sigma = \Gamma, X, \quad (5)$$

$$\frac{1}{q} \frac{dJ_n^\sigma(z)}{dz} = U_n^\sigma(z), \quad \sigma = \Gamma, X, \quad (6)$$

$$\frac{1}{q} \frac{dJ_p(z)}{dz} = U_p(z), \quad (7)$$

where  $\psi(z)$  is the potential,  $\epsilon(z)$  is the position dependent permittivity,  $q$  is the elementary charge,  $n^\sigma(z)$  and  $p(z)$  are the  $\Gamma$  and  $X$  electron and hole concentrations,  $N_T(z)$  is the sum of the ionized donor and acceptor concentrations, and  $J_n^\sigma(z)$  and  $J_p(z)$  refer to the  $\Gamma$  and  $X$  electron and hole current

densities, respectively.  $U_n^\sigma(z)$  denotes the sum of the recombination and generation rates for the  $\Gamma$ - $X$  electrons and holes, respectively.  $J_n^\sigma(z)$  and  $J_p(z)$  are given by

$$J_n^\sigma(z) = -q\mu_n^\sigma(z) \left[ n^\sigma(z) \frac{d\psi(z)}{dz} - \frac{1}{\theta} \frac{dn^\sigma(z)}{dz} \right], \quad \sigma = \Gamma, X, \quad (8)$$

$$J_p(z) = -q\mu_p(z) \left[ p(z) \frac{d\psi(z)}{dz} + \frac{1}{\theta} \frac{dp(z)}{dz} \right], \quad (9)$$

where  $\theta$  is the reciprocal of the thermal voltage and  $\mu_n^\sigma(z)$  and  $\mu_p(z)$  are the  $\Gamma$ - $X$  electron and hole mobilities respectively. Both the Shockley-Read-Hall and direct recombination models have been included in the model; these are expressed as<sup>28,31</sup>

$$R_{\text{SRH},n}^\sigma = \frac{n_i^2 - n^\sigma p}{\tau_p(n^\sigma + n_i) + \tau_n(p + n_i)}, \quad \sigma = \Gamma, X, \quad (10)$$

$$R_{\text{SRH},p}^\sigma = \sum_{\sigma} \frac{n_i^2 - n^\sigma p}{\tau_p(n^\sigma + n_i) + \tau_n(p + n_i)}, \quad (11)$$

$$R_D = B(n, p)(n_i^2 - pn), \quad (12)$$

Here  $B(n, p)$  is the carrier dependent radiative recombination coefficient,  $\tau_p$  and  $\tau_n$  are the nonradiative hole and electron lifetimes, and  $p_i$  and  $n_i$  are the intrinsic carrier concentrations dependent on trap position and occupancy.<sup>31</sup> In Eqs. (5)–(11), the superscript  $\sigma$  runs over both the  $\Gamma$  and  $X$  electrons.

The conduction and valence band positions and offsets were deduced via the band parameter model similar to that of Sutherland and Hauser.<sup>32</sup> This model utilizes the energy band alignment of Anderson<sup>33</sup> to calculate the band parameters and uses the vacuum energy level as the reference for the electrostatic potential. Hence, the  $\Gamma$  and  $X$  conduction and valence band discontinuities are given by the difference in the electron affinities of two adjacent materials. Although more sophisticated models<sup>34,35</sup> have been developed to predict the conduction band offsets of the  $(\text{Al}_x\text{Ga}_{1-x})_y\text{In}_{1-y}\text{P}$  material system, we use the Anderson model for its ease of use numerically. Comparison of the conduction band offsets predicted using this model, e.g.,  $\sim 0.16$  eV for the heterojunction  $(\text{Al}_{0.3}\text{Ga}_{0.7})_{0.48}\text{In}_{0.52}\text{P}/(\text{Al}_{0.7}\text{Ga}_{0.3})_{0.48}\text{In}_{0.52}\text{P}$ , agrees well with that predicted by other methods.<sup>34,35</sup> Furthermore, in this investigation and the reviewed experimental results it is the extent of the enhancement to these conduction band offsets that is the primary focus.

An adapted Newton iteration algorithm was used to solve the MDD equations. In this solution scheme Eqs. (5)–(8) were expressed in the following way:

$$\begin{bmatrix} J^{pp} & J^{pn_\Gamma} & J^{pn_X} & J^{p\psi} \\ J^{n_\Gamma p} & J^{n_\Gamma n_\Gamma} & J^{n_\Gamma n_X} & J^{n_\Gamma \psi} \\ J^{n_X p} & J^{n_X n_\Gamma} & J^{n_X n_X} & J^{n_X \psi} \\ J^{\psi p} & J^{\psi n_\Gamma} & J^{\psi n_X} & J^{\psi \psi} \end{bmatrix} \begin{bmatrix} \delta p \\ \delta n_\Gamma \\ \delta n_X \\ \delta \psi \end{bmatrix} = - \begin{bmatrix} F_p(p, n_\Gamma, n_X, \psi) \\ F_{n_\Gamma}(p, n_\Gamma, n_X, \psi) \\ F_{n_X}(p, n_\Gamma, n_X, \psi) \\ F_\psi(p, n_\Gamma, n_X, \psi) \end{bmatrix}, \quad (13)$$

where the first matrix on the left-hand side is the Jacobian, the second corresponds to the update of the simulation variables, and the right-hand side corresponds to the three continuity equations and Poisson's equation. Under low bias conditions, the partial derivatives in the Jacobian were evaluated analytically for each update iteration (i.e., Newton's method), giving quadratic convergence. However, at forward biases greater than approximately 1 V this approach did not converge quadratically for each bias increment, normally set at 0.1 V. This is due to the analytic expressions of the partial derivatives becoming a bad initial guess of the solution at the next applied voltage step. To reduce iteration time two different methods were employed: (i) a feedback mechanism that systematically decreased the voltage step size so that the partial derivatives of the Jacobian become a "better" guess and (ii) employing a modified Broyden method<sup>36</sup> to approximate the partial derivatives within the Jacobian.<sup>28</sup> It was found that for applied voltages between 1.3 and 1.8 V the modified Broyden method produced faster convergence and the same voltage step size could be maintained.

## V. OPTIMIZATION PROCEDURE

The overall optimization procedure is an iterative process between RC and the MDD equation sets and is illustrated in the form of a flowchart in Fig. 4. An initial MQB structure is input into the RC routine where its layer widths are optimized to find the best reflectivity characteristic, namely, a high effective enhancement with no evidence of  $\Gamma$  or  $X$  electron transmission below 99% of the maximal value of the reflection probability, i.e., 1. When a good structure is located, the MQB is inserted within the laser device and the MDD routine is used to generate the energy bands at an operating bias of 2 V. The position of the energy bands of the initial inputted MQB will have been distorted due to charge injection; thus, the reflectivity probability is recalculated to confirm if the good reflectivity characteristics remain. If they do not the MQB parameters are readjusted. If they do persist the layer widths of the MQB are sequentially increased and decreased by one monolayer and the reflection probabilities compared to determine if a stable enhancement has been established. In this context "stable" refers to the condition that all reflectivity spectra should exhibit enhancement characteristics similar to those of the original biased MQB. This rigorous selection process is undertaken to minimize the effects of interface roughness and intrinsic experimental tolerances induced in the fabrication of such structures.<sup>37</sup>

These material issues have a detrimental influence on both experimental and theoretical MQB performances. From cross-sectional scanning tunneling microscopy (XSTM) measurements conducted by Teng *et al.*<sup>38</sup> on previous

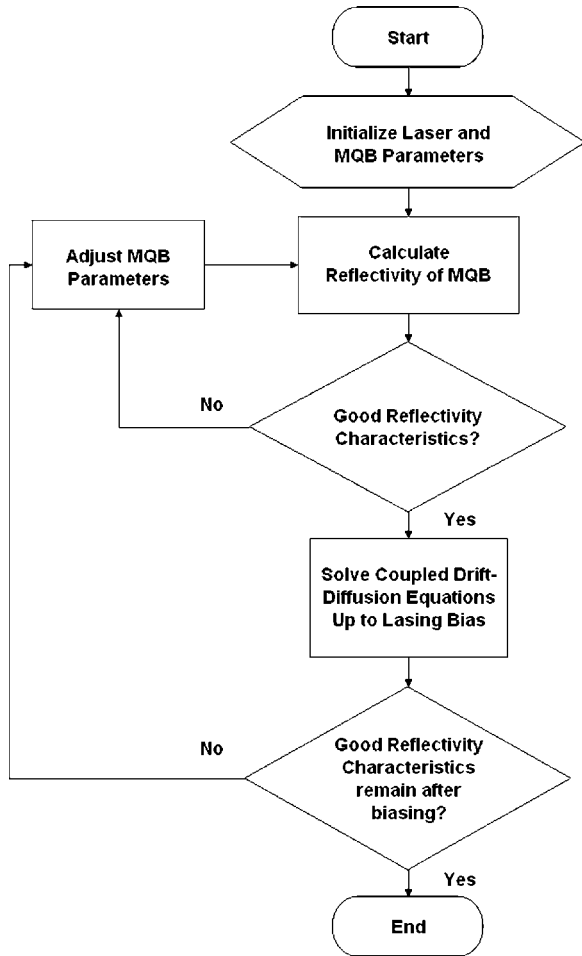


FIG. 4. Flowchart indicating the major steps of the MQB optimization iterative process.

AlInP/GaInP and AlInP/AlGaInP MQB laser structures it was found that there was considerable interface roughness at each heterojunction caused by dopant interdiffusion across the MQB, which destroys its periodic nature. To counter these effects two measures were taken: (i) a minimum layer width of 14 monolayers was used and (ii) the MQB well and barrier layers were set to aluminum contents of 0.3 and 0.7, respectively. The first condition was set because it was the authors' opinion that this was the limiting width of the consecutive varying AlGaInP alloy layers which could be grown accurately and consistently at the time of manufacture. Also, fluctuations of one monolayer could be incorporated within the optimization procedure. The second condition reduces the number of dopants available for interdiffusion at each heterointerface and results in more abrupt and defined superlattice layer.

However, limiting the MQB with these conditions limits the extent of its potential impact in the following ways: (i) the extent of the forbidden miniband is a function of the thinness of the superlattice wells, i.e., for maximum impact thin wells are needed, and (ii) the intrinsic height of the conduction band offset is a maximum at an aluminum content of 1, hence, reducing the percentage of aluminum content reduces further the already small conduction band offset. Thus, the choices of the minimum layer width and layer

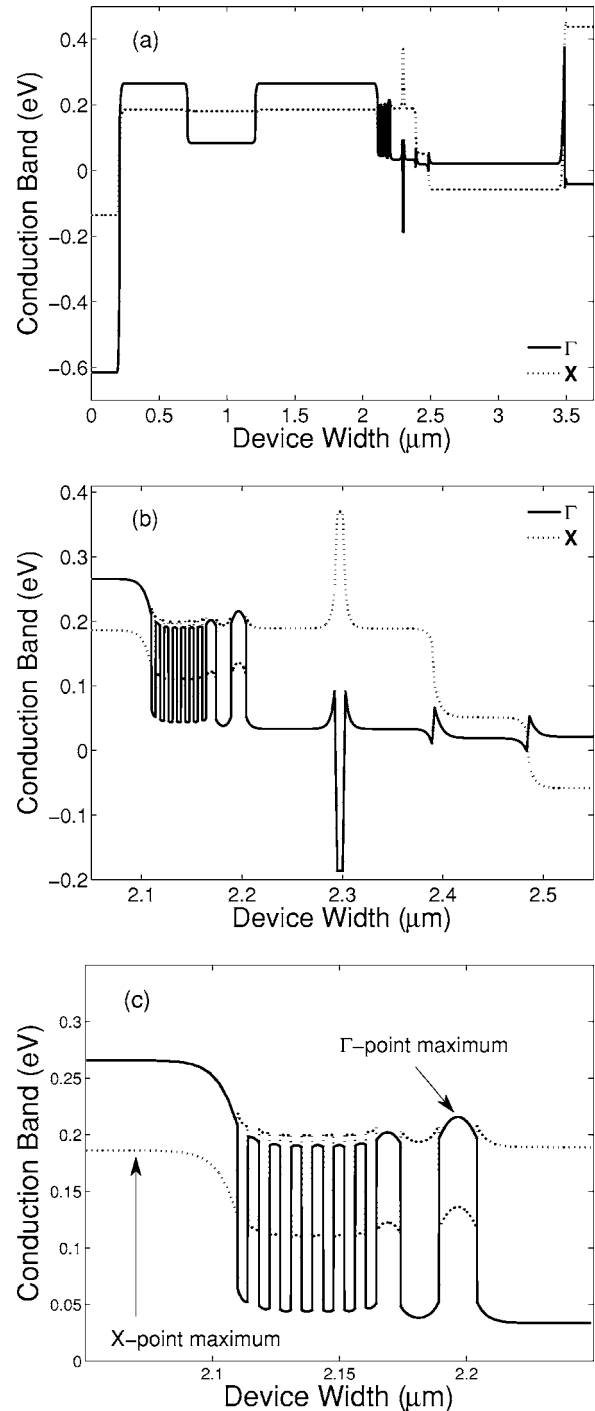


FIG. 5. Plots indicating the relative position of the two conduction bands at an applied bias of 2 V. (a) Whole laser device incorporating MQB 1. (b) Enlargement of the energy band diagram around the active region of the device to exemplify the extent of band bending across MQB 1. (c) Enlargement of the MQB region.

composition of the superlattice are a compromise of two opposing factors and were chosen to balance the growth issues on one hand against the desired reflectivity properties on the other.

## VI. RESULTS

Using the methods described in Secs. IV and V the laser structure incorporating MQB 1 was modeled and the effec-

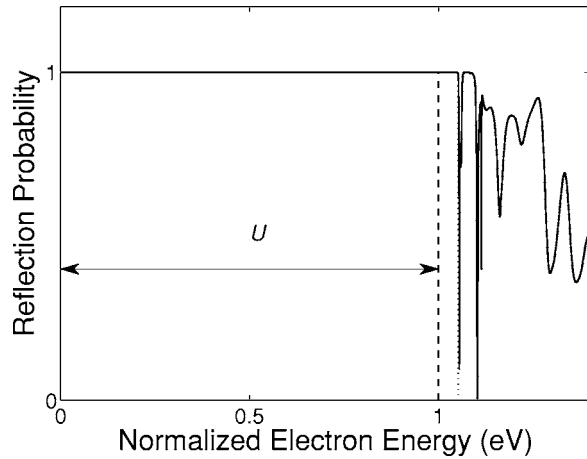


FIG. 6. Reflectivity profile of MQB 1 where the band structure has been generated using the MDD routine. The effective enhancement  $U_e$  (dotted line) indicates an increase of 4% to the normalized barrier height  $U$  (intermittent line).

tive conduction band offset enhancement,  $U_e$ , it imparted deduced. Figure 5(a) displays the calculated energy band profile at an applied bias of 2 V for the whole device. Additionally, Figs. 5(b) and 5(c) display magnifications around the active and MQB regions, respectively. Comparison of the conduction bands predicted by the solution of solely Poisson's equation and that of the MDD [Figs. 1(b) and 5(c), respectively] reveals considerable underestimation of the band bending across all material interfaces by the former model. This can be expected as no charge diffusion is accounted for. It is this effect that has lowered the position of the MQB relative to the adjacent  $p$ -doped cladding layer. Consequently, the X-band maximum [displayed in Fig. 5(c)] has been raised in energy with respect to that same point marked in Fig. 1(b), resulting in a reduced effective enhancement. However, the extent of the band bending across the MQB region itself is very similar in both cases and supports the former model being a good first approximation.

Figure 6 displays the total reflectivity of MQB 1, which predicts an effective enhancement  $U_e$  of 4% to the X-band maximum. This value corresponds to an enhancement of 7 meV and compares favorably to that inferred experimentally by Sobiesierski *et al.* (5 meV).

Gaining confidence from these initial results MQB 1 was again reoptimized using the procedure detailed above to produce a second MQB (MQB 2) capable of reflecting higher energy electrons. MQB 2 consists of three thick initial material layers of 159, 129, and 120 Å width, respectively, where the second is a well of composition of  $(\text{Al}_{0.3}\text{Ga}_{0.7})_{0.48}\text{In}_{0.52}\text{P}$  surrounded by two barriers of composition of  $(\text{Al}_{0.7}\text{Ga}_{0.3})_{0.48}\text{In}_{0.52}\text{P}$ . The superlattice of the MQB comprises six well/barrier pairs of composition of  $(\text{Al}_{0.3}\text{Ga}_{0.7})_{0.48}\text{In}_{0.52}\text{P}/(\text{Al}_{0.7}\text{Ga}_{0.3})_{0.48}\text{In}_{0.52}\text{P}$ , where each individual layer is 42 Å in width. Figure 7(a) displays the calculated energy band structure for the full laser device with the optimized MQB included under a working bias of 2 V. Figures 7(b) and 7(c) display a magnification of the conduction band around the active and adjacent  $p$ - and  $n$ -doped cladding regions and of the MQB region, respectively.

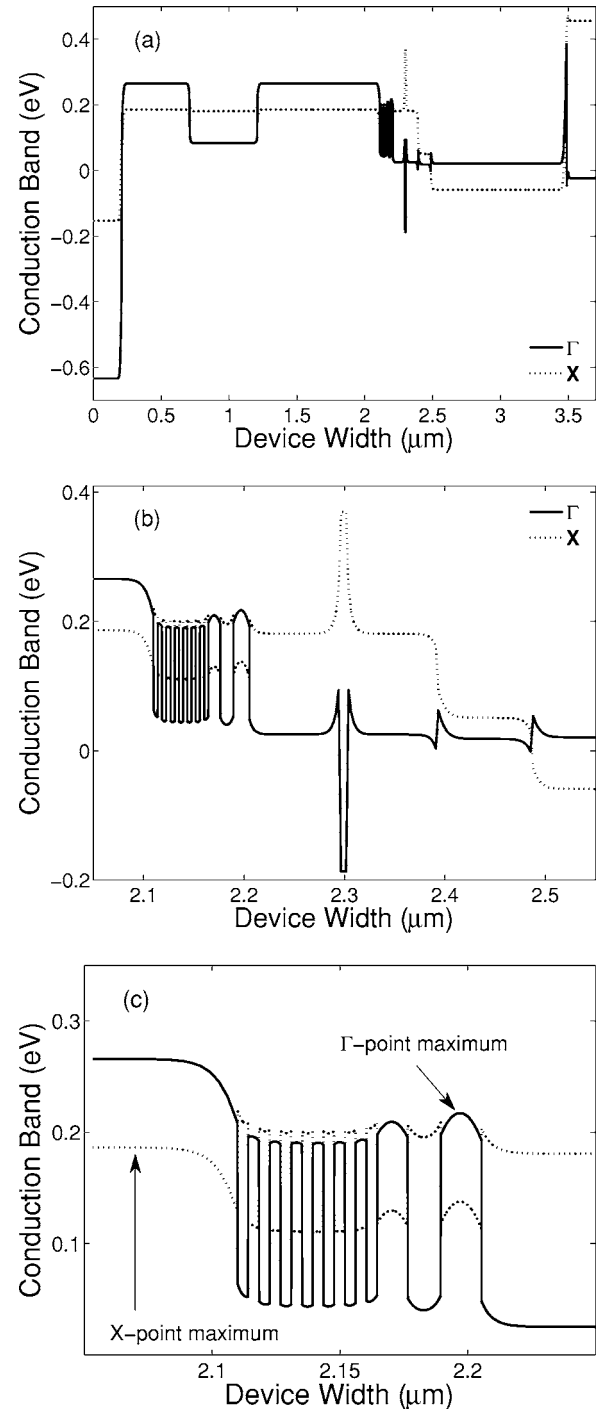


FIG. 7. (a)  $\Gamma$  and X conduction bands across the laser device incorporating MQB 2 at operating voltage. (b) Enlargement of the energy band diagram around the active region of the device to exemplify the extent of band bending across MQB 2. (c) Enlargement of the MQB region.

Figure 8 displays the total reflectivity profile associated with a MQB 2 and is normalized with respect to the X-point maximum,  $U$  [see Fig. 7(c)], and predicts a 7% enhancement,  $U_e$ , with respect to this point. This translates to a 13 meV increase to the intrinsic conduction band offset.

Due to the indeterministic magnitude associated with the mixing parameter  $\alpha$ , Fig. 9 displays two supplementary reflectivity profiles in addition to that calculated from the optimized MQB structure. Plots (a)–(c) display the calculated reflectivity spectra where the magnitude of the mixing pa-



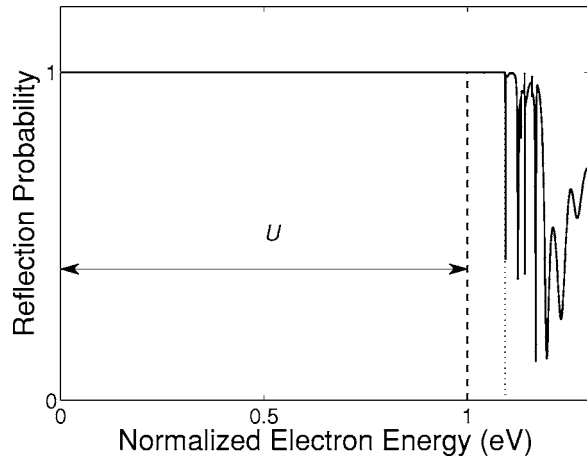


FIG. 8. Calculated reflectivity profile of MQB 2 indicating an effective enhancement  $U_e$  (dotted line) of 7% with respect to the normalized barrier height  $U$  (intermittent line).

parameter has been varied by  $\pm 30\%$  of its original value. Each complementary reflectivity profile exhibits identical enhancements,  $U_e$ , to that of the original (Fig. 8) and no evidence of additional transmission features is evident. This demonstrates that the solutions are insensitive to the magnitude of the mixing parameter.

## VII. SUMMARY

A theoretical model has been presented in an attempt to bridge the gap between theoretically predicted and experimentally measured effective enhancements due to the inclusion of MQB structures within red-emitting AlGaInP laser diodes. Very good agreement between experimentally deduced and theoretically predicted effective enhancements

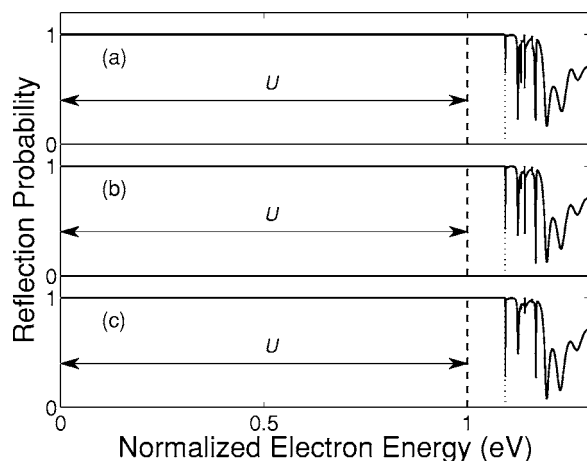


FIG. 9. Reflectivity spectra of the proposed MQB 2 structure under lasing conditions, where plots (a), (b), and (c) correspond to the magnitudes 0.1, 0.155, and 0.22 eV Å of the intervalley mixing parameter  $\alpha$ .

was found. The MQB structure was redesigned using the updated numerical scheme and predicted an increase to the intrinsic conduction band offset of 7%.

- <sup>1</sup>D. P. Bour, D. W. Treat, R. L. Thornton, R. S. Geels, and D. F. Welch, *IEEE J. Quantum Electron.* **29**, 1337 (1993).
- <sup>2</sup>S. A. Wood, C. H. Molloy, P. M. Smowton, P. Blood, and C. C. Button, *IEEE J. Quantum Electron.* **36**, 742 (2000).
- <sup>3</sup>K. Iga, H. Uenohara, and F. Koyama, *Electron. Lett.* **22**, 1008 (1986).
- <sup>4</sup>R. de L. Kronig and W. J. Penney, *Proc. R. Soc. London* **A130**, 499 (1930).
- <sup>5</sup>T. Takagi, F. Koyama, and K. Iga, *Jpn. J. Appl. Phys., Part 1* **31**, 197 (1992).
- <sup>6</sup>T. Takagi, F. Koyama, and K. Iga, *IEEE J. Quantum Electron.* **27**, 1511 (1991).
- <sup>7</sup>M. Toivonen, P. Savolainen, and M. Pessa, *Semicond. Sci. Technol.* **11**, 1923 (1996).
- <sup>8</sup>T. Takagi and K. Iga, *IEEE Photonics Technol. Lett.* **4**, 1377 (1992).
- <sup>9</sup>J. Rennie, M. Watanabe, M. Okajima, and G. Hatakoshi, *Electron. Lett.* **28**, 150 (1992).
- <sup>10</sup>A. P. Morrison, J. D. Lambkin, C. J. van der Poel, and A. Valster, *IEEE Photonics Technol. Lett.* **8**, 849 (1996).
- <sup>11</sup>A. P. Morrison *et al.*, *IEEE J. Quantum Electron.* **33**, 1338 (1997).
- <sup>12</sup>P. Raisch *et al.*, *Appl. Phys. Lett.* **74**, 2158 (1999).
- <sup>13</sup>M. R. Brown, K. S. Teng, A. Kestle, P. M. Smowton, P. Blood, P. A. Mawby, and S. P. Wilks, *Appl. Surf. Sci.* **234**, 434 (2004).
- <sup>14</sup>T. Takagi, F. Koyama, and K. Iga, *Electron. Lett.* **27**, 1081 (1991).
- <sup>15</sup>C. S. Chang, Y. K. Su, S. J. Chang, P. T. Chang, Y. R. Wu, K. H. Huang, and T. P. Chen, *IEEE J. Quantum Electron.* **34**, 77 (1998).
- <sup>16</sup>D. P. Bour, in *Quantum Well Lasers*, edited by P. S. Zory (Academic, New York, 1993), p. 415.
- <sup>17</sup>M. P. C. M. Krijn, *Semicond. Sci. Technol.* **6**, 27 (1991).
- <sup>18</sup>P. M. Smowton and P. Blood, *IEEE J. Quantum Electron.* **31**, 2159 (1995).
- <sup>19</sup>A. Sobiesierski, I. C. Sandall, P. M. Smowton, P. Blood, A. B. Krysa, M. R. Brown, K. S. Teng, and S. P. Wilks, *Appl. Phys. Lett.* **86**, 021102 (2005).
- <sup>20</sup>P. Blood, G. M. Lewis, P. M. Smowton, H. D. Summers, J. D. Thomson, and J. Lutti, *IEEE J. Sel. Top. Quantum Electron.* **9**, 1275 (2003).
- <sup>21</sup>H. C. Liu, *Appl. Phys. Lett.* **51**, 1019 (1987).
- <sup>22</sup>A. P. Morrison and J. D. Lambkin, *Opt. Eng. (Bellingham)* **33**, 3926 (1994).
- <sup>23</sup>D. Landheer, H. C. Lui, M. Buchanan, and R. Stoner, *Appl. Phys. Lett.* **54**, 1784 (1989).
- <sup>24</sup>A. C. Marsh, *Semicond. Sci. Technol.* **1**, 320 (1986).
- <sup>25</sup>A. C. Marsh, *IEEE J. Quantum Electron.* **23**, 371 (1987).
- <sup>26</sup>A. C. Marsh and J. C. Inkson, *J. Phys. C* **17**, 6561 (1984).
- <sup>27</sup>H. K. Gummel, *IEEE Trans. Electron Devices* **ED-27**, 455 (1964).
- <sup>28</sup>S. Selberherr, *Analysis and Simulation of Semiconductor Devices* (Springer-Verlag Wien, New York, 1984), Chap. 8.
- <sup>29</sup>M. S. Lundstrom and R. J. Schuelke, *IEEE Trans. Electron Devices* **ED-30**, 1151 (1983).
- <sup>30</sup>Z.-M. Li, S. P. McAllister, and C. M. Hurd, *Semicond. Sci. Technol.* **5**, 408 (1990).
- <sup>31</sup>C. Snowden, *Introduction to Semiconductor Device Modelling* (World Scientific, Singapore, 1986), Chap. 2.
- <sup>32</sup>J. E. Sutherland and J. R. Hauser, *IEEE Trans. Electron Devices* **ED-24**, 363 (1977).
- <sup>33</sup>R. L. Anderson, *Solid-State Electron.* **30**, 341 (1962).
- <sup>34</sup>X. H. Zhang, S. J. Chua, and W. J. Fan, *Appl. Phys. Lett.* **73**, 1098 (1998).
- <sup>35</sup>D. Vignaud and F. Mollot, *J. Appl. Phys.* **93**, 384 (2003).
- <sup>36</sup>D. Kincaid and W. Cheney, *Numerical Analysis*, 2nd ed. (Brooks-Cole, Belmont, MA, 1996), Chap. 2.
- <sup>37</sup>K. S. Teng, M. R. Brown, A. Kestle, P. Smowton, P. Blood, S. Pinches, P. A. Mawby, and S. P. Wilks, *Appl. Surf. Sci.* **190**, 284 (2002).
- <sup>38</sup>K. S. Teng, M. R. Brown, A. Kestle, P. Smowton, P. Blood, S. Pinches, P. A. Mawby, and S. P. Wilks, *J. Appl. Phys.* **98**, 033525 (2005).